Higher Recovery and Better Energy Dissipation at Faster Strain Rates in Carbon Nanotube Bundles: An *in-Situ* Study

Siddhartha Pathak,[†,*] Ee J. Lim,[†] Parisa Pour Shahid Saeed Abadi,[‡] Samuel Graham,[‡,§] Baratunde A. Cola,[‡,§] and Julia R. Greer[†]

[†]Materials Science, California Institute of Technology (Caltech), Pasadena, California, United States and [‡]George W. Woodruff School of Mechanical Engineering, and [§]School of Materials Science and Engineering, Georgia Institute of Technology, Atlanta, Georgia, United States

ABSTRACT

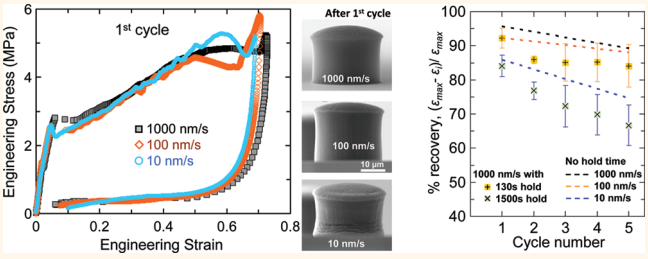

We report mechanical behavior and strain rate dependence of recoverability and energy dissipation in vertically aligned carbon nanotube (VACNT) bundles subjected to quasi-static uniaxial compression. We observe three distinct regimes in their stress—strain curves for all explored strain rates from 4×10^{-2} down to 4×10^{-4} /sec: (1) a short initial elastic section followed by (2) a sloped plateau with characteristic wavy features corresponding to buckle formation and (3) densification characterized by rapid stress increase. Load—unload cycles reveal a stiffer response and virtually 100% recoverability at faster strain rates of 0.04/sec, while the response is more compliant at slower rates, characterized by permanent localized buckling and significantly reduced recoverability. We propose that it is the kinetics of attractive adhesive interactions between the individual carbon nanotubes within the VACNT matrix that governs morphology evolution and ensuing recoverability. In addition, we report a 6-fold increase in elastic modulus and gradual decrease in recoverability (down to 50%) when VACNT bundles are unloaded from postdensification stage as compared with predensification. Finally, we demonstrate energy dissipation capability, as revealed by hysteresis in load—unload cycles. These findings, together with high thermal and electrical conductivities, position VACNTs in the "unattained-as-of-to-date-space" in the material property landscape.

KEYWORDS: vertically aligned carbon nanotubes · compression · mechanical properties · energy storage · recovery

Resilience, or a material's ability to recover back to its original dimensions after deformation, is a key criterion in assessing lifetime reliability of material systems. If a material exhibits time-dependent deformation, that is, viscoelasticity, like vertically aligned carbon nanotube (VACNT) bundles,[1,2] it is common for its stress—strain behavior to exhibit a hysteresis loop upon cyclical loading, thus dissipating energy in every cycle.[3] Here we show that both recoverability and energy dissipation in VACNTs are strongly dependent on strain-rate, attaining their maxima by loading at faster rates. Specifically, we find that when compressed at the faster strain rates of 4×10^{-2}/sec, the VACNT bundles recover virtually back to their original dimensions, while at the slower deformation rates of 4×10^{-4}/sec, they remain permanently deformed (<86% recovery), as evidenced by their post-mortem morphology containing localized buckles. The resilience of the VACNT samples is further compromised when they are loaded to beyond densification threshold strains of $\varepsilon \geq 0.65-0.7$ for all strain rates.

It has been shown previously that compressive behavior of VACNT bundles is strongly affected by variations in their complex hierarchical morphology, collective intertube interactions, and inherent property gradients, which in turn are controlled by the synthesis techniques.[4] In part, this is evidenced by the wide range of mechanical properties reported for VACNTs, such as variations in modulus and buckling strength that range anywhere from sub-MPa[1,5] to tens of MPa[6−8] to GPa[9,10] levels. Another marked difference among existing reports is the ability (or lack thereof) of some VACNT microstructures to recover from large deformations; with some exhibiting superior creep recovery,[1−3,11] while others deform permanently even at modest strains.[8,12−14] The ability of VACNT bundles to dissipate energy while maintaining their dimensional stability with >80% recovery has suggested their future use for energy storage applications such as viscoelastic rubbers and foams.[2,15]

In this work ~30 μm × 30 μm (height × diameter) cylindrical pillars of VACNTs were grown by atmospheric pressure chemical

* Address correspondence to pathak@caltech.edu, siddharthapathak@gmail.com.

Received for review October 24, 2011 and accepted February 14, 2012.

Published online February 14, 2012
10.1021/nn300376j

vapor deposition (APCVD) and tested both in air and in an *in situ* nanomechanical instrument inside of a scanning electron microscope (SEM) under compressive cyclic loading (up to five load–unload cycles) at three different displacement rates of 10, 100, and 1000 nm/s, which correspond to strain rates of 0.0004, 0.004, and 0.04/sec, respectively (see Methods). The stress–strain responses of VACNTs were measured using quasi-static uniaxial compression experiments on these cylindrical specimens[1,3,12] as in this configuration the deformation occurs under a relatively homogeneous stress field, which is in contrast to quasi-static nanoindentation[10,16,17] or dynamic impact testing methods[18–20] where the presence of strong strain gradients obscure stress–strain calculations. The *in situ* observations in SEM during the experiments allow for simultaneous correlation between morphological evolution in VACNTs and their stress–strain behavior.[12,21]

As shown in the representative stress–strain curve at 100 nm/sec in Figure 1, these pillars exhibit remarkable resilience (>90% recovery), with virtually no discernible changes from their original morphology (compare Figures 1b and 1f) even after cycling to relatively high strains of 70–80%. Furthermore, their load-unload trajectories are characterized by a considerable hysteresis loop, implying energy dissipation during deformation.

It has been proposed that some of the factors leading to nearly full recovery and energy dissipation in VACNT bundles can be attributed to their hierarchical microstructure[1,2,12] (Figure 1b). At the lowest magnification (bottom SEM image Figure 1b) the VACNT pillar has a distinctive muffin-like shape, with a bulbous top caused by the particular APCVD growth process (see Methods). APCVD VACNT pillars of such short heights also tend to have a lower density (and hence, a more compliant structure) at the bottom closer to the substrate compared to taller APCVD forests.[22] This is evident in the darker hue in the bottom $\sim 2\ \mu$m of the pillar in Figure 1b. Not surprisingly, upon compression the first buckling instability forms at this location (Figure 1c). Compared to other CNT structures, VACNT bundles are characterized by a significant number (~millions) of CNTs arrayed in a nominally vertical alignment growing perpendicularly to the support substrate, as seen at higher (micrometer level) magnifications (Figure 1b, second image from bottom). However the long strands of individual CNTs intertwine in the course of their growth, which becomes apparent at higher magnifications (Figure 1b, third image from bottom). Upon careful examination, in their as-grown states some tubes appear prebuckled and/or prebent, and the favorable contact energy between the tubes is thought to balance the bending strain energy of their arrangement, resulting in a more stable low energy configuration.[6] This is in contrast to arrays of VACNTs that are short and/or sparse enough that each individual CNT stands alone.[23] At still higher magnifications (nanometer length scales, see top TEM image in Figure 1b), individual, discrete CNTs dominate the mechanical performance with details like CNT diameter, number of walls *etc*. governing their deformation.

Despite their complex, hierarchical microstructure, the general compressive behavior of VACNTs is akin to that of typical open-cell foams,[24] as evident from Figure 1a. In the spirit of the overall open foam-like response, the stress–strain curves of VACNTs are characterized by 3 distinct regimes: (1) initial linear elastic region, followed by (2) an oscillatory plateau region, where each undulation is associated with localized buckling events, extending to the strains of ~65–70%, beyond which the stress steeply increases due to (3) densification. At the scale of its constituents, however, the response of VACNTs is quite different from that of traditional foams. In VACNT bundles, the postelastic compressive strain is accommodated entirely *via* the formation of lateral folds or buckles usually close to the bottom of the bundle, while the remaining portion remains virtually unscathed.[12] This is in contrast to traditional foams, where cell-edge bending and cell collapse are primarily responsible for the elastic–plastic foam response.[24,25] In our VACNT samples (Figure 1c), the formation of the first buckle at the bottom signals the transition from elastic to plateau regime. The postelastic plateau region in the stress–strain curve also shows marked differences from that of an open cell foam response, as evidenced by its nonzero positive slope and wave-like shape, where each undulation can be traced to subsequent buckling events (videos S1, S2 and S3 in the Supporting Information). The positive slope of the plateau region has been attributed to the presence of a vertical property gradient in the VACNT pillars.[3,12] The plateau region continues to slope upward until ~50% strain, where a pronounced kink forms approximately at the midheight of the pillar, leading to softening. This kink formation marks the end of the plateau, after which the stress–strain behavior shifts into the densification regime characterized by a steep stress increase over a very small strain.

The initial portion of the "elastic" regime (at very low strains $\varepsilon \leq 0.05$ shown in Figure 1a) is often affected by experimental artifacts like the small initial misalignment between the indenter head and the micropillar, as well as top surface imperfections. Here, the deformation of the entire bulbous top of the VACNT pillars is fully contained within this elastic region, rendering quantitative analysis of this section of the stress–strain impractical. Therefore, we focus our analysis on the postelastic deformation only (see Methods).

Figure 1a also shows the effect of load-unload cycling on the mechanical behavior of VACNT micropillars compressed at 100 nm/s. It is evident that the first cycle is distinctly different from all subsequent

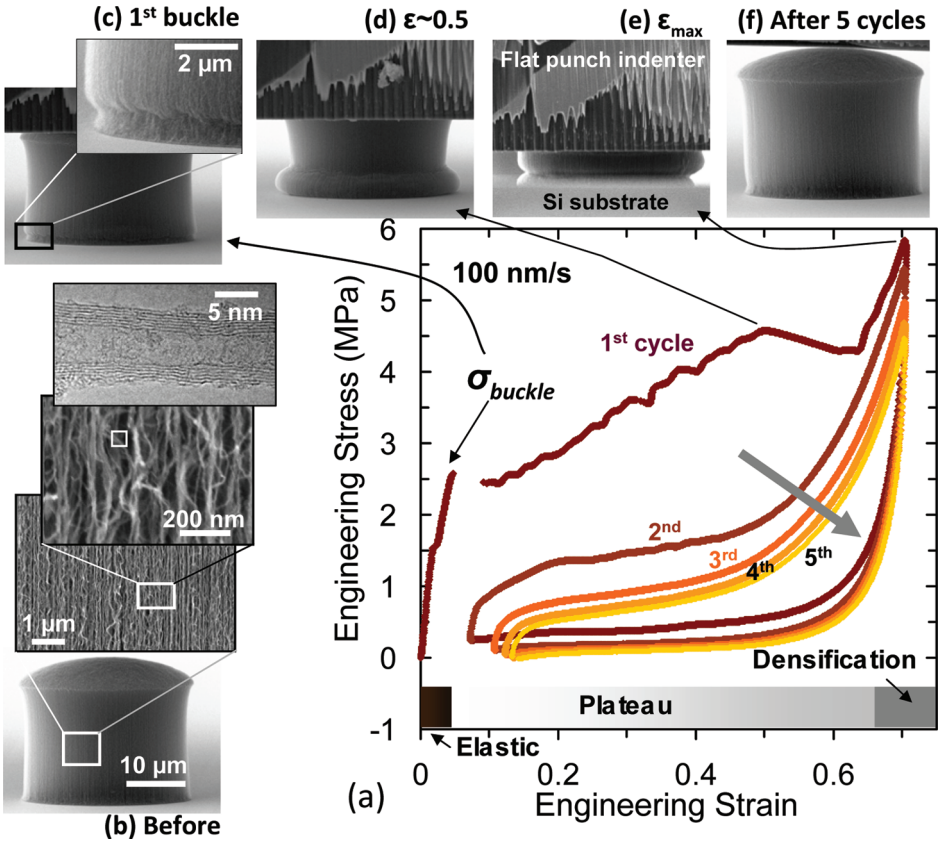

Figure 1. (a) 5 load–unload cycles in compression of a VACNT micro-muffin by a flat punch diamond indenter at 100 nm/s showing 3 distinct regimes; elastic, plateau, and densification. The first buckling instability, formed at the bottom of the pillar shown in (c), marks the start of the sloped plateau region where buckles form progressively. Densification typically starts after the large buckle at $\varepsilon \sim 0.5$ (d) and continues till ε_{max} (e). Successive load–unload cycles to the same strain in (a) also reveal a gradual drop in stress and recovery every cycle, suggesting progressive damage accumulation in the material. Micrographs in (b) reveal the hierarchical morphology of VACNTs, which consist of nominally vertical aligned CNTs at low magnification, and a complex intertwined network at higher magnification. Individual multiwalled CNTs are visible in the TEM image. SEM pictures are taken at a 86 deg tilt angle.

loading cycles, which are self-consistent. For example the buckling stress as well as the plateau stress for the first loading are much higher than those in the latter cycles. It is also apparent that both the amount of hysteresis, corresponding to the energy dissipated every cycle, and the recovered strain after unloading decrease with increasing cycle number.

Under varying displacement rates (Figure 2), further differences in the amount of recovery come to light. As seen from the first unloading segment, recoverability appears to increase at higher strain rates when unloaded from the same nominal maximum strain. This is also evident from the post-mortem SEM images, which clearly show permanent deformation and remnants of buckles in the samples compressed at the slowest 10 nm/s displacement rate, while samples compressed at higher rates appear identical to their initial state, that is, lacking any evidence of deformation. Note also that the plateau region in the samples deformed at the slowest rate shows more pronounced undulations, corresponding to more buckling events occurring at this rate (compare Supporting Information videos S1, S2, and S3). All of this suggests a strong dependence

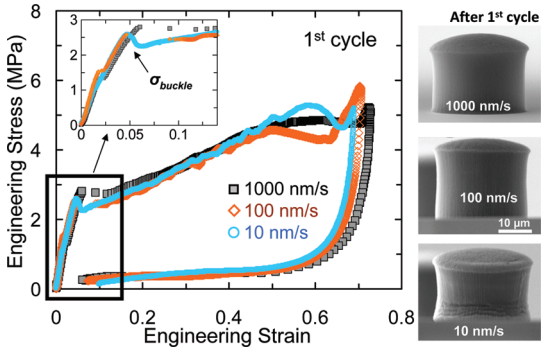

Figure 2. Tests at different displacement rates showing more pronounced buckling signatures and lesser recovery at the lower rates. SEM images in the figure are taken at a 86° tilt angle.

of deformation commencement on strain rate. Further, our demonstration of nearly full recovery and a lack of morphological damage in VACNTs deformed at the highest tested strain rates may have significant implications for its use as protective materials.

Stiffness changes, measured as the elastic modulus calculated from the initial unloading slope in the

stress−strain curves, as a function of displacement rate and maximum strain, are shown in Figure 3. For a particular displacement rate (for example 100 nm/s, orange diamonds in Figure 3a), the moduli obtained in such a way change considerably depending on the maximum strains attained before unloading. Thus while the moduli in the plateau regime start at a low value (around 120 MPa at $\varepsilon = 0.1$ for 100 nm/s), they increase steadily to ~175 MPa up to the strain of $\varepsilon \sim 0.5$. This evolution in the modulus mirrors the trends shown in the shape of the stress−strain curve for the first load−unload cycle shown in Figures 1 and 2. As seen from Figure 1a and 1d, the strain at $\varepsilon \approx 0.5$ is associated with the formation of a large buckle in the middle of the pillar, and is followed by a decrease in the slope of the stress−strain curve. Following a similar trend, the modulus also drops to 145 MPa at strains higher than 0.5. Once the densification threshold strain is reached ($\varepsilon \geq 0.65-0.7$), the modulus increases rapidly with strain to values of up to 2−4 times than that in the predensification regime.

The variations in the modulus between the different regimes are also revealed in Figure 3b, where the results from the pre- and postdensification regimes are summarized separately. The considerably higher moduli in the densification regime, for example, increasing by more than a factor of 2 from 177 ± 11 MPa to 385.1 ± 149 MPa in the first cycle for the fastest 1000 nm/s displacement rate, are likely the effect of the significant increase in density due to compaction of the sample. In addition both pre- and postdensification regimes in Figure 3b show an increasing trend in the stiffness with faster rates, a behavior considered typical for viscoelastic solids.[26] Thus the fastest deformation rate of 1000 nm/s consistently results in the higher moduli in both regimes. Repeated cycling further exacerbates the localization of deformation into folds, leading to stiffness degradation (Figure 3b).

The % recovery shows a similar correlation with both the displacement rate and the maximum attained strains (Figure 4). Figure 4a shows recovery to be virtually 100% when unloaded from elastic regime, >90% when unloaded from the plateau regime, and only 50−80% when unloaded from strains in the densification segment ($\varepsilon \geq 0.65-0.7$). The recovery in the postdensification regime is seen to decrease gradually from >80% to ~50% with increasing strain levels. Similar to the modulus, samples deformed at the slowest 10 nm/s rate are most permanently deformed (*i.e.*, least recovered, with 86.9 ± 2% recovery for the first cycle), while those compressed at the fastest (1000 nm/s) rate show a high 95.6 ± 3% recovery. While the recovery prior to densification decreases gradually with cycling, after densification the recovery drops sharply in the second cycle and then stabilizes to a relatively lower value (Figure 4b). We find that the error bars in the data within the postdensification regime (right image in Figure 4b) are

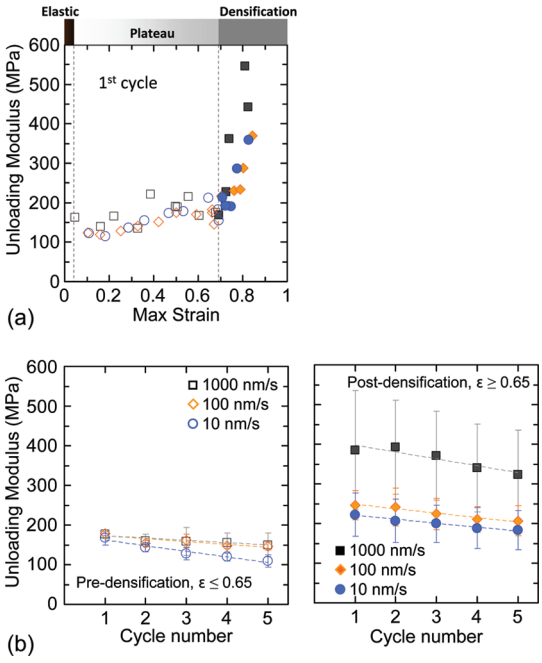

Figure 3. (a) Changes in the unloading modulus as a function of the maximum strains attained before unloading showing a response similar to the material's stress−strain behavior. (b) Modulus values (average ± standard deviation) at different load−unload cycles as a function of their displacement rates in the predensification (open symbols) and postdensification (filled symbols) regimes.

significantly larger than those before densification, likely a result of the % recovery being a strong function of the unloading strain in this regime. Also since the VACNT pillars compressed at the fastest rate of 1000 nm/s were subjected to higher strains (Figure 4a), they recovered less than the ones compressed at the slower 100 nm/s rate in the postdensified regime (Figure 4b).

Our viscoelastic analysis (see Figure S1 in the Supporting Information) indicates that the time constant associated with the recovery of the VACNTs is very short, on the order of ~0.1 s (see also ref 12), and significantly below the deformation rates studied in our work. We also verified the same by loading the VACNTs *in situ* in SEMentor at various displacement rates (of 10, 100, and 1000 nm/s) and then quickly unloading the indenter head, which confirmed that VACNT recovery occurs very rapidly; at the frame capture rate of 30 frames/sec the entire recovery was completed within a single frame at unloading.

Interestingly, relative recovery, defined as recovery compared with the previous, as opposed to initial, cycle (Figure 4c), shows an identical trend for pre and postdensified regimes. By the third cycle, data across all three rates shows ~100% relative recovery. This suggests that in spite of the differences in their absolute values, the recovery in the VACNTs follows a deterministic (rather than stochastic) mechanism for all deformation rates.

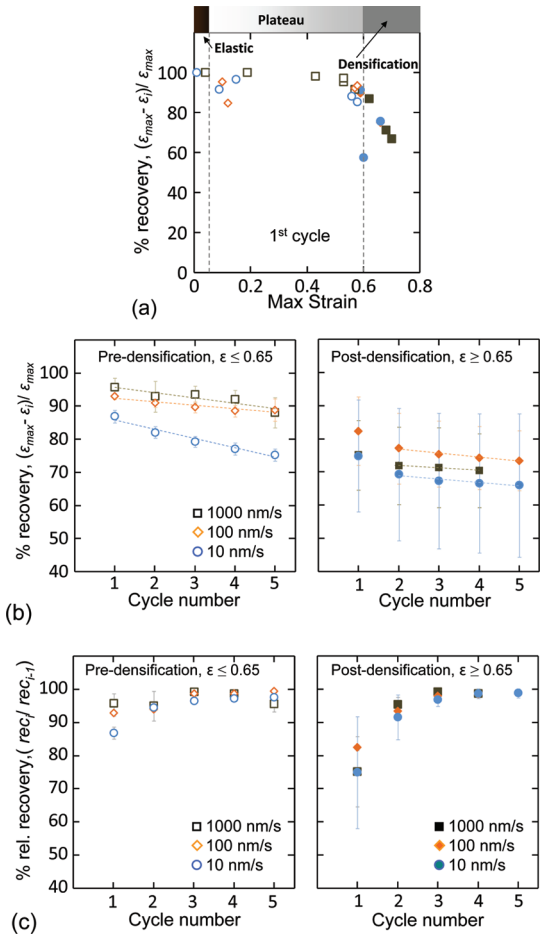

Figure 4. (a) Percent recovery as a function of maximum strain attained before unloading showing higher recovery in the predensification regime (open symbols) while the recovery progressively decreases beyond densification (filled symbols). This is shown more clearly in panels (b) where recovery is higher at faster rates. (c) Similarity of changes in relative recovery values suggest that the process of mechanical damage accumulation is consistent among different rates. Note that tests in the postdensification regime for the 1000 nm/s rate in (b) and (c) had only four load–unload cycles.

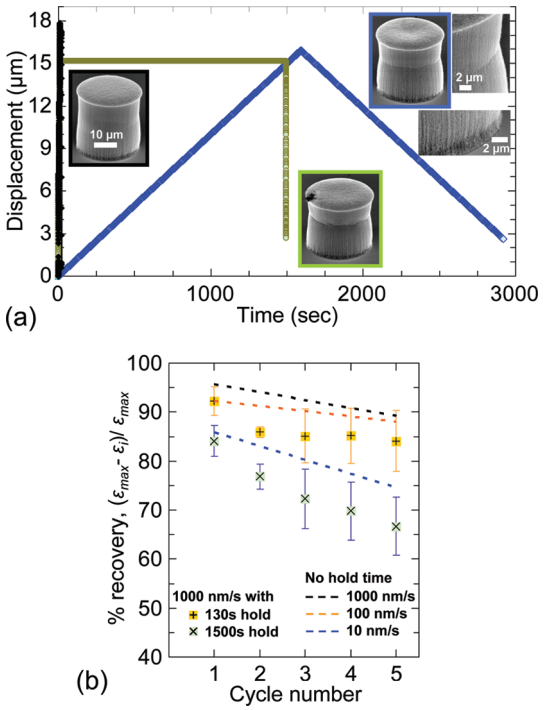

Figure 5. (a) Schematic of test designs showing displacement–time plots for three different cases: a fast load-unload test at 1000 nm/s (black curve), a slow load-unload test at 10 nm/s (blue), and a fast load-unload test at 1000 nm/s with a 1500 s hold time at maximum displacement (green). All samples were loaded to a nominal maximum strain of $\varepsilon \approx 0.6$. Inset micrographs show the postcompression images of the VACNT micropillars taken at a 60 deg tilt angle after 5 such load–unload cycles. (b) Percent recovery as a function of cycle number for tests with and without hold times. The trend lines for the tests without hold time is reproduced from the data in Figure 4b of the manuscript.

While a robust mathematical description of the time dependence of VACNT recovery is beyond the scope of this work, the basic phenomenological process may be understood as follows. When compressed at the lower deformation rates, the individual CNT struts rearrange themselves by twisting, bending, *etc.*, in response to the applied compressive load, thereby coming into close contact with one another. This type of individual strut reconfiguration is not unreasonable in a high-entropy deformation process (*i.e.*, many different configurations are available at each time step). Several groups have now shown that VACNTs deform similarly to foams[3,12,24] likely due to their open cell structure created by interwoven and intertwined tubes, which act as supporting struts.[3,12] In addition, CNTs are inherently "sticky," experiencing an adhesive driving force due to van der Waals interactions.[27] Therefore, in the course of compression at the slower rates, an ever-increasing number of individual struts coalesce by coming into close proximity of one another, thereby forming localized densified regions (*i.e.*, buckles). Importantly, the adhesion process appears to be largely irreversible; that is, the adhesion driving force overrides the stored elastic energy upon unloading. This implies that after unloading the buckles remain even while undergoing elastic recovery. This all is in contrast to the deformation at higher rates, where the entire structure recovers completely, with no evidence of the buckles' presence upon unloading (see Figures 1, 2, and 5). We believe that this behavior stems from an insufficient interaction time between individual tubes to come in contact with one another. This results in a significantly reduced contact intertubular area as compared with the slowly deformed case, and hence leads to much lower adhesion. Compression at higher rates is likely a lower-entropy process since there are fewer configurations available during each time step, and therefore less intertubular contact occurs, leading to the lack of localized "zipped-up" densified buckles.[2,11,15,16]

Thus, it stands to reason that if different VACNT micropillars were allowed similar amounts of time for

the reconfiguration to occur, they should exhibit similar percent recovery for all loading rates. This is shown schematically in Figure 5a, where loading the sample to $\varepsilon \approx 0.6$ (predensification regime) at the fast rate of 1000 nm/s and then holding it at the max load for ~1500 s (green curve) ensures that it spends an equivalent amount of time before unload as the sample deformed at 10 nm/s test (blue curve). Figure 5b clearly shows that a hold time of ~130 s decreases the recovery for the 1000 nm/s displacement rate tests from 96 to 92% in the first cycle, while a longer hold time of ~1500 s brings it down even further to 86%. Note that these reduced percent recovery values are similar to those for the slower 100 and 10 nm/s rates, respectively (see also Figure 4b). Pillars subjected to the additional hold times at maximum strain show a steeper decrease in their recovery in cycles after the second load–unload (Figure 5b), implying that the longer time spent at a high strain is more detrimental to recovery than a gradual increase in strain to a maximum value over the entire time period. The above results suggest that it is the time spent by the VACNTs under high strains, rather than the loading history, that determines the permanence of their deformation.

The postcompression images in Figure 5a also demonstrate a similar signature: while a VACNT micropillar deformed at 1000 nm/s with no hold is virtually indistinguishable from its original configuration (left inset micrograph bordered in black), those micropillars deformed for longer periods of time have accordion-like morphologies, with vertically stacked folds along their heights (inset micrograph in the middle and right, bordered in green and blue, respectively), for both slow and fast loading rates.

The combination of recoverability and viscoelasticity in VACNTs results in their path-dependent load–unload behavior upon cycling, manifested as hysteresis loops shown in Figure 1a. The fraction of energy dissipated during the process can be calculated as the loss coefficient η (see Methods), shown in Figure 6a as a function of cycling. From this figure it is apparent that the loss coefficient is significantly higher for the first load–unload cycle (η = 0.13–0.15) after which η drops sharply (to values of 0.07 and lower). Subsequent load-unload cycles cause the amount of energy dissipated to decrease steadily with increased cycling. η also appears to be strain dependent, and is maximized at the fastest 1000 nm/sec rate, similar to the trends noted for modulus and recovery. No particular differences were noticed between the pre- and postdensification regimes in terms of the loss coefficient values. These results match well with the tan δ measurements (see Figure S1 in Supporting Information)

The strain rate dependence of the recovery and energy dissipation in the VACNTs appears to follow a strong correlation with their increased stiffness at the faster rates. Higher stiffness at faster rates leads to a corresponding

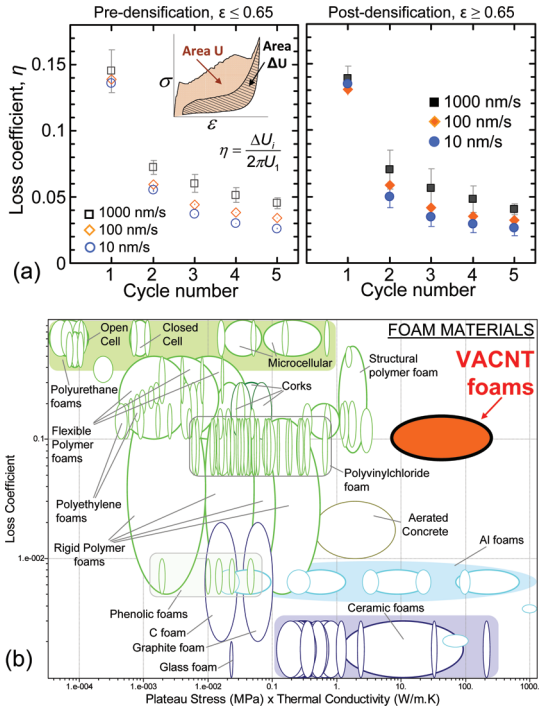

Figure 6. (a) The loss coefficient values as a function of load–unload cycles showing better energy dissipation at higher rates. (b) Ashby chart of loss coefficient (energy dissipation) *vs* plateau stress (signifying the foam strength) multiplied by thermal conductivity of foam materials showing the VACNT system as an ideal candidate for combining the advantages of both metallic and polymeric foams. Using electrical conductivity instead of thermal also generates a very similar plot.

increase in the buckling stress (Figures 1 and 2), which increases from 2.43 ± 0.16 MPa at 10 nm/s to 2.55 ± 0.2 MPa at 100 nm/s to 2.69 ± 0.12 MPa at 1000 nm/s (average ± standard deviation of 10 or more measurements). Usually, the buckling stress defines the beginning of the plateau region, and since the plateau region accounts for the largest fraction of the area under the stress–strain curve, a higher buckling stress corresponds to greater energy absorption in the material and the ability to sustain higher stresses during the extended deformability in this plateau region. Energy dissipation in VACNT bundles, on the other hand, is achieved upon unloading when the VACNTs transform back to their nearly original alignment (unbuckle) by dissipating the excess energy. Since energy dissipated is calculated as a function of the area under the load–unload curve, this value is inherently linked to the amount of recovery of the unloading curve. Hence the rate-dependent damping behavior of the VACNTs can also be explained by a similar line of reasoning as the VACNT recovery described earlier.

CONCLUSION

In summary, we demonstrate that VACNT cylindrical bundles grown by CVD technique exhibit unique deformation properties, namely resilience, deformability, and energy dissipation, all of which increase at faster strain

rates. We hypothesize that it is the inability of individual CNTs in the VACNT matrix to reconfigure and come into contact with one another, promoting adhesion and localized buckle formation, which governs recoverability. Specifically, we find that the deformation at slower strain rates results in the formation of localized, permanent buckles along the pillar height, while faster strain rates render the individual struts' interaction times insufficient for adhesion, leading to nearly full recovery. As such, these materials appear to combine the best aspects of different foam characteristics, such as their ability to switch between various buckled morphologies which makes them capable of undergoing large strains of *ca.* 60−80% without generating damaging peak stresses (similar to metallic foams[25]), as well as their high resilience and close to 100% recovery upon load release leading to a higher energy dissipation (as in polymeric foams[24]). This combination of desirable properties suggests their potential use in protective applications. Even more importantly, their multifunctional nature, high electrical (comparable to copper) and thermal (similar to metals) conductivities,[28,29] and relative ease of manufacture identifies VACNT bundles as a completely new class of material systems entering the "white space" in the material property chart, as shown in Figure 6b.[30]

METHODS

CNT Pillar Growth. Nominally *ca.* 30 μm × 30 μm (height × diameter) size micropillars of VACNTs were grown using an atmospheric pressure chemical vapor deposition (APCVD) technique in a commercial (CVD) system (Black Magic Pro 4″, Aixtron SE).[22] Photolithography and a photoresist lift-off process were employed to pattern a trilayer catalyst of Ti (30 nm)/Al (10 nm)/Fe (3 nm) deposited by electron beam evaporation on Si substrates to seed the growth of micropillars. A gas mixture of 160/100/7500 sccm of $C_2H_2/H_2/N_2$ was used to maintain the chamber pressure at 750 mbar during growth, which occurred at ∼750 °C. Multiwall CNTs, with an average diameter of 8.8 ± 2.1 nm (average ± standard deviation), were produced by this process. The average mass density (CNT mass divided by volume) was measured to be ∼80 mg/cm^3. The muffin-like shape of the VACNT micropillars is an artifact of this APCVD growth process that remains unexplained. High magnification SEM shows that the bulb top is formed by the ends of nanotubes, suggesting that the particular bulb top shape was caused by lower CNT growth rates near the rim of the pillars. Transmission electron microscopy (TEM) images of the APCVD-VACNTs were taken in a JEOL 4000EX machine.

Compression Tests. Vertically oriented cylindrical pillars with an aspect ratio (height/diameter ≈ 30 μm/30 μm) were synthesized for cyclic compression tests. The compression experiments were performed using the XP module of Agilent's nanoindenter G200 with custom Testworks software control methods as described in ref 12. Compression tests were performed in air using a diamond flat punch of ∼120 μm diameter at different displacement rates: 10, 100, and 1000 nm/s, which correspond to strain rates of 0.0004, 0.004, and 0.04/sec, respectively. Typically five load−unload cycles were performed at each strain level. The maximum strains reached for the pillars were varied from 10 to 80%. A minimum of 10 tests were conducted at each compression rate.

As has been observed before by several research groups,[6,12] CNTs frequently adhere to the diamond indenter tip, which results in slightly negative values of load during the final stages of unloading in some cases (see Figure 1a). This effect is further intensified by the additional CNTs present in the protruded bulbous head of the pillar. To mitigate this effect each cycle was unloaded to only 10% of the max load in the previous cycle. In addition to maintaining a positive value of the load (and stress), this approach also helps to prevent loss of contact between the indenter tip and the pillar during loading and hence maintain the cyclic nature of the tests.

***In-Situ* SEM Experiments.** To capture the local deformation events occurring during compression, *in situ* tests were also conducted inside our custom built mechanical deformation system, SEMentor,[31] which is composed of a nanomechanical dynamic contact module (Agilent Corp.) inside a SEM (Quanta 200, FEI). Tests in the SEMentor were conducted with a ∼60 μm × 80 μm conductive diamond flat punch in a similar manner to the G200. The compression axis in the SEMentor is inclined by about 86° with respect to the electron beam, thus allowing continuous observation of the deformation morphology of the VACNT micropillar during the loading/unloading cycle, simultaneously with the acquisition of the load and displacement values. The SEM observations were recorded as a video file and later synchronized with the engineering stress−strain curve to provide a one-to-one correlation between each video frame and its corresponding position on the stress−strain curve (see videos S1, S2, and S3 in the Supporting Information). Testing parameters in the SEMentor were identical to that of the in-air G200 tests.

However, tests in the SEMentor differ from those in the G200 in some key aspects, such as the SEMentor tests are conducted in a vacuum environment with an electron beam focused on the pillar, and the VACNT micropillars are in a horizontal configuration (gravity acting perpendicular to the compression axis) inside the SEMentor. For this study, results from the SEMentor were used only for visualization purposes; all data analyses were performed on tests conducted in the G200 nanoindenter machine.

Data Analysis. Engineering stress (σ) and strain (ε) were calculated using the initial diameter (d_0) and height (h_0) of the VACNT micropillar, where h_0 = [total height of the pillar] − [height of the bulbous top], along with the corrected load (p_{corr}) and displacement (u_{corr}) following the procedure in ref 12. Frictional forces between the VACNT pillar and the indenter head were ignored.[32,33]

$$\sigma = \frac{p_{corr}}{\pi d_0^2/4'} \quad \varepsilon = \frac{u_{corr}}{h_0} \tag{1}$$

Note that eq 1 ignores the height of the bulbous top of the pillar when calculating engineering strain ε, thus assuming that the deformation of the protruded pillar top has little or no effect in the stress−strain response of the VACNT pillar. This assumption is motivated by evidence from the video files S1, S2 and S3 in the Supporting Information. As seen from these videos the deformation of the entire bulbous top of the pillar is concentrated entirely in the "elastic" portion of the loading response, while the rest of the pillar comes in full contact with the indenter head at the beginning of the "plateau" regime (see Figure 1a). We also verified this effect by monitoring the continuous stiffness measurement (CSM) signal during the test, which showed that the point of full contact of the pillar with the indenter head—and hence the entire deformation of the protruded head of the pillar—is within the initial "elastic" portion of the test. Additional validation of our approach is provided by the fact that the modulus (E) values measured as the slope of the initial 30% of the unloading stress−strain curve calculated using eq 1 (see Figure 3 in the manuscript) match closely with the values calculated from the viscoelastic tests

(Figure S1 in the Supporting Information). If h_0 is taken to be the total height of the pillar (rather than being corrected for the additional height of the bulb), the modulus values are overestimated by around 25%.

The percentage recovery (R) values in the VACNT micropillar samples were measured as amount of strain recovered at the end of every cycle with respect to the maximum applied strain; that is, $R = (\varepsilon_{max} - \varepsilon_{unload})/\varepsilon_{max}$, where ε_{max} is the maximum strain level at the end of loading and ε_{unload} is the strain after unloading to 10% of the max load in the respective cycle. Similarly the percentage relative recovery values were measured as the strain recovered in every cycle (i) compared to its previous one ($i-1$); that is, Relative Recovery $= R^i/R^{i-1} = (\varepsilon^i_{max} - \varepsilon^i_{unload})/(\varepsilon^{i-1}_{max} - \varepsilon^{i-1}_{unload})$ (Figure 4).

The loss coefficient, η (a dimensionless quantity), measures the degree to which a material dissipates energy and is calculated as[30]

$$\eta = \frac{\Delta U_i}{2\pi U_1}, \quad U = \int_0^{\sigma_{max}} \sigma \, d\varepsilon, \quad \Delta U = \oint \sigma \, d\varepsilon \qquad (2)$$

where U_1 is the elastic energy stored in the material when it is loaded elastically to a stress σ_{max} in the first cycle, and ΔU_i is the energy dissipated in the ith load−unload cycle (see Figure 6a). We point out that in eq 2 ΔU_i is normalized with respect to the area of the first loading cycle (*i.e.*, a constant value). Instead, normalizing the area of the hysteresis loop with respect to the area of the respective ith cycle can also provide useful information about the damping behavior of the VACNTs, as shown in the Supporting Information Figure S2.

A zero hold time at maximum load was used in all cases, except for the test shown in Figure 5. For the tests shown in Figure 5a three different test setups were used: the black curve denotes a VACNT micropillar loaded at a fast rate of 1000 nm/s up to a strain of ~0.6 (*i.e.*, in the predensification regime) and then unloaded at the same rate, the blue curve shows the same for a slow 10 nm/s loading−unloading rate, while the VACNT micropillar shown in the green curve was loaded at the fastest rate of 1000 nm/s to a maximum strain of $\varepsilon \approx 0.6$, held for 1500 s at that maximum strain level, and then unloaded again at 1000 nm/s. In other words, both VACNTs micropillars shown in green (fast 1000 nm/s loading rate) and blue (slow 10 nm/s loading rate) spent the same amount of time under compression before unload: $(\text{loading time} + \text{hold time})_{green,1000nm/s} = (\text{loading time})_{blue,10\ nm/s}$. Five such load−unload cycles were carried out for each pillar. In another similar set of experiments the VACNT micropillars were loaded at the fastest rate of 1000 nm/s, then held for 130 s at the maximum strain and subsequently unloaded, effectively bringing the time-spent-before-unload to the same level as in the case of a slower 100 nm/s load-unload test with no hold.

Conflict of Interest: The authors declare no competing financial interest.

Acknowledgment. The authors acknowledge S. Hutchens for helpful insights and guidance, N. Mohan for data analysis, financial support from the Georgia Institute of Technology Foundation through the Joseph Anderer Faculty Fellowship, and the Institute for Collaborative Biotechnologies (ICB) for financial support through Grant W911NF-09-0001 from the U.S. Army Research Office. The content of the information does not necessarily reflect the position or the policy of the Government, and no official endorsement should be inferred. S.P. gratefully acknowledges support from the W. M. Keck Institute for Space Studies Postdoctoral Fellowship program for this work. The authors acknowledge critical support and infrastructure provided for this work by the Kavli Nanoscience Institute at Caltech.

Supporting Information Available: Three *in situ* videos of the VACNT micropillar compressions, synchronized with their respective engineering stress−strain curves; video files S1, S2, and S3 illustrate the VACNT micropillar deformations at 10, 100, and 1000 nm/s which are shown at 100, 25, and 1 times their original speeds, respectively; viscoelastic characterization of the VACNT micropillars (Figure S1) and the details of the loss coefficient measurement (Figure S2). This material is available free of charge *via* the Internet at http://pubs.acs.org.

REFERENCES AND NOTES

1. Suhr, J.; Victor, P.; Sreekala, L. C. S.; Zhang, X.; Nalamasu, O.; Ajayan, P. M. Fatigue Resistance of Aligned Carbon Nanotube Arrays under Cyclic Compression. *Nat. Nanotechnol.* **2007**, *2*, 417–421.
2. Xu, M.; Futaba, D. N.; Yamada, T.; Yumura, M.; Hata, K. Carbon Nanotubes with Temperature-Invariant Viscoelasticity from −196 degrees to 1000 degrees C. *Science* **2010**, *330*, 1364–1368.
3. Cao, A. Y.; Dickrell, P. L.; Sawyer, W. G.; Ghasemi-Nejhad, M. N.; Ajayan, P. M. Super-Compressible Foamlike Carbon Nanotube Films. *Science* **2005**, *310*, 1307–1310.
4. Kumar, M.; Ando, Y. Chemical Vapor Deposition of Carbon Nanotubes: A Review on Growth Mechanism and Mass Production. *J. Nanosci. Nanotechnol.* **2010**, *10*, 3739–3758.
5. Tong, T.; Zhao, Y.; Delzeit, L.; Kashani, A.; Meyyappan, M.; Majumdar, A. Height Independent Compressive Modulus of Vertically Aligned Carbon Nanotube Arrays. *Nano Lett.* **2008**, *8*, 511–515.
6. Mesarovic, S. D.; McCarter, C. M.; Bahr, D. F.; Radhakrishnan, H.; Richards, R. F.; Richards, C. D.; McClain, D.; Jiao, J. Mechanical Behavior of a Carbon Nanotube Turf. *Scr. Mater.* **2007**, *56*, 157–160.
7. Qiu, A.; Bahr, D. F.; Zbib, A. A.; Bellou, A.; Mesarovic, S. D.; McClain, D.; Hudson, W.; Jiao, J.; Kiener, D.; Cordill, M. J. Local and Non-local Behavior and Coordinated Buckling of CNT Turfs. *Carbon* **2011**, *49*, 1430–1438.
8. Zhang, Q.; Lu, Y. C.; Du, F.; Dai, L.; Baur, J.; Foster, D. C. Viscoelastic Creep of Vertically Aligned Carbon Nanotubes. *J. Phys. D: Appl. Phys.* **2010**, *43*, 315401.
9. Deck, C. P.; Flowers, J.; McKee, G. S. B.; Vecchio, K. Mechanical Behavior of Ultralong Multiwalled Carbon Nanotube Mats. *J. Appl. Phys.* **2007**, *101*, 23512.
10. Pathak, S.; Cambaz, Z. G.; Kalidindi, S. R.; Swadener, J. G.; Gogotsi, Y. Viscoelasticity and High Buckling Stress of Dense Carbon Nanotube Brushes. *Carbon* **2009**, *47*, 1969–1976.
11. Xu, M.; Futaba, D. N.; Yumura, M.; Hata, K. Carbon Nanotubes with Temperature-Invariant Creep and Creep-Recovery from −190 to 970 °C. *Adv. Mater.* **2011**, *23*, 3686–3691.
12. Hutchens, S. B.; Hall, L. J.; Greer, J. R. *In Situ* Mechanical Testing Reveals Periodic Buckle Nucleation and Propagation in Carbon Nanotube Bundles. *Adv. Funct. Mater.* **2010**, *20*, 2338–2346.
13. Zbib, A. A.; Mesarovic, S. D.; Lilleodden, E. T.; McClain, D.; Jiao, J.; Bahr, D. F. The Coordinated Buckling of Carbon Nanotube Turfs under Uniform Compression. *Nanotechnol.* **2008**, *19*, 175704–1−7.
14. Cao, C.; Reiner, A.; Chung, C.; Chang, S.-H.; Kao, I.; Kukta, R. V.; Korach, C. S. Buckling Initiation and Displacement Dependence in Compression of Vertically Aligned Carbon Nanotube Arrays. *Carbon* **2011**, *49*, 3190–3199.
15. Gogotsi, Y. High-Temperature Rubber Made from Carbon Nanotubes. *Science* **2010**, *330*, 1332–1333.
16. Bradford, P. D.; Wang, X.; Zhao, H.; Zhu, Y. T. Tuning the Compressive Mechanical Properties of Carbon Nanotube Foam. *Carbon* **2011**, *49*, 2834–2841.
17. Maschmann, M. R.; Zhang, Q.; Wheeler, R.; Du, F.; Dai, L.; Baur, J. *In Situ* SEM Observation of Column-like and Foam-like CNT Array Nanoindentation. *ACS Appl. Mater. Interfaces* **2011**, *3*, 648–653.
18. Daraio, C.; Nesterenko, V. F.; Jin, S.; Wang, W.; Rao, A. M. Impact Response by a Foamlike Forest of Coiled Carbon Nanotubes. *J. Appl. Phys.* **2006**, *100*, 64309.
19. Misra, A.; Greer, J. R.; Daraio, C. Strain Rate Effects in the Mechanical Response of Polymer-Anchored Carbon Nanotube Foams. *Adv. Mater.* **2008**, *20*, 1–5.
20. Raney, J. R.; Fraternali, F.; Amendola, A.; Daraio, C. Modeling and *in Situ* Identification of Material Parameters for Layered Structures Based on Carbon Nanotube Arrays. *Compos. Struct.* **2011**, *93*, 3013–3018.
21. Yaglioglu, O. Carbon Nanotube Based Electromechanical Probes. Ph.D. Thesis, Massachusetts Institute of Technology, Cambridge, MA, 2007.

22. Abadi, P. P. S. S.; Hutchens, S.; Taphouse, J. H.; Greer, J. R.; Cola, B. A.; Graham, S. The Effect of Morphology on the Micro-compression Response of Carbon Nanotube Forests. *Carbon* **2011**submitted for publication.
23. Waters, J. F.; Riester, L.; Jouzi, M.; Guduru, P. R.; Xu, J. M. Buckling Instabilities in Multiwalled Carbon Nanotubes under Uniaxial Compression. *Appl. Phys. Lett.* **2004**, *85*, 1787–1789.
24. Gibson, L. J.; Ashby, M. F., *Cellular Solids: Structure and Properties*; Cambridge University Press: UK, 1999.
25. Gibson, L. J. Mechanical Behavior of Metallic Foams. *Annu. Rev. Mater. Sci.* **2000**, *30*, 191–227.
26. Lakes, R. S., *Viscoelastic Solids*; CRC Press, Boca Raton, FL, 1998.
27. Ruoff, R. S.; Tersoff, J.; Lorents, D. C.; Subramoney, S.; Chan, B. Radial Deformation of Carbon Nanotubes by van der Waals Forces. *Nature* **1993**, *364*, 514–516.
28. Baxendale, M. In *The Physics and Applications of Carbon Nanotubes*; 12th International School on Condensed Matter Physics: Contemporary Trends in Condensed Matter Physics and Technology, 1−6 Sept. 2002, USA, Kluwer Academic Publishers: Norwell, MA, 2003; pp 657−659.
29. Hu, X. J.; Padilla, A. A.; Xu, J.; Fisher, T. S.; Goodson, K. E. 3-Omega Measurements of Vertically Oriented Carbon Nanotubes on Silicon. *J. Heat Transfer* **2006**, *128*, 1109–1113.
30. Ashby, M. F. *Materials Selection in Mechanical Design*, 3rd ed.; Butterworth-Heinemann: Oxford, UK, 2005.
31. Kim, J.-Y.; Greer, J. R. Tensile and Compressive Behavior of Gold and Molybdenum Single Crystals at the Nano-Scale. *Acta Mater.* **2009**, *57*, 5245–5253.
32. Tu, J. P.; Jiang, C. X.; Guo, S. Y.; Fu, M. F. Micro-friction Characteristics of Aligned Carbon Nanotube Film on an Anodic Aluminum Oxide Template. *Mater. Lett.* **2004**, *58*, 1646–9.
33. Tu, J. P.; Zhu, L. P.; Hou, K.; Guo, S. Y. Synthesis and Frictional Properties of Array Film of Amorphous Carbon Nanofibers on Anodic Aluminum Oxide. *Carbon* **2003**, *41*, 1257–1263.